SLAC-PUB-14513

# A Heteroepitaxial Perovskite Metal-Base Transistor

T. Yajima[1], Y. Hikita[1], and H. Y. Hwang[1,2,3]

[1]*Department of Advanced Materials Science, University of Tokyo, Kashiwa, Chiba 277-8561, Japan*

[2]*Japan Science and Technology Agency, Kawaguchi, Saitama 332-0012, Japan*

[3] *Department of Applied Physics and SLAC Photon Science, Stanford University, Stanford, CA 94305, USA*

**"More than Moore"[1] captures a concept for overcoming limitations in silicon electronics, by incorporating new functionalities in the constituent materials. Perovskite oxides are candidates due to their vast array of physical properties in a common structure. They also enable new electronic devices based on strongly-correlated electrons[2]. The field effect transistor[3] and its derivatives have been the principal oxide devices investigated thus far[4-6], but another option is available in a different geometry: if the current is perpendicular to the interface, the strong internal electric fields generated at back-to-back heterojunctions can be used for oxide electronics, analogous to bipolar transistors[7]. Here we demonstrate a perovskite heteroepitaxial metal-base transistor[8] operating at room temperature,**

**enabled by interface dipole engineering[9]. Analysis of many devices quantifies the evolution from hot-electron[10] to permeable-base[11] behaviour. This device provides a platform for incorporating the exotic ground states of perovskite oxides, as well as novel electronic phases at their interfaces[12-15].**

The initial and still very active study of three-terminal complex oxide devices primarily uses the field effect transistor (FET)[4]. Despite successes in some oxides, the FET intrinsically suffers from the requirement of large electric fields needed to induce conductivity in many perovskites[16]. These high fields have been partially mitigated by the use of ferroelectric polarisation[5] or electric double layer structures[6]. Historically, however, it is noteworthy that before the demonstration of the FET[3], the first transistors were based not on electron transport parallel to the active interface, but rather perpendicular to them. The very first transistor, for example, used two Au Schottky contacts to *p*-type Ge[17]. This format has a natural advantage for our purposes, since the internal electric fields generated at Schottky junctions can be orders of magnitude larger than can be externally applied across a gate dielectric, and transconductance is controlled by the base current, not gate voltage.

A metal-base transistor[8] consists of a semiconductor/metal/semiconductor trilayer, where each layer functions as the emitter, base, and collector, respectively, and two Schottky junctions are formed. The heteroepitaxial structure studied here (Fig. 1a) consisted of a manganite metal layer between titanate semiconductors. The fundamental transport process of a metal-base transistor is parameterised by the current gain $\alpha$, the ratio of the collector current $I_C$ to that injected from the emitter $I_E$ [18]. Ideally, $I_C$ is dominated by current transferred from the emitter, resulting in typical transistor operation as a current source with large output impedance at the collector. In practice, however, leakage current at the base-collector (BC) junction may contribute to $I_C$, which reduces output impedance substantially, even inhibiting transistor operation at room temperature in some cases[19].

This issue appeared in the present study, as seen from the current-voltage characteristics of the BC and base-emitter (BE) junctions at 300 K (Fig. 1b). Rectifying behaviour indicates Schottky diodes are formed at both interfaces. In the active mode of the transistor, the BC diode is reverse-biased to electrically isolate the collector from the base, and the BE diode is forward biased to inject carriers. It is evident that the leakage current at the BC junction (red arrow) is as large as the injection current at the BE junction (blue triangle). As a result, no significant transconductance could be found in devices using this geometry.

To suppress this leakage current, the BC junction barrier height was raised by atomically engineering the BC interface[9]. Prior to depositing $La_{0.7}Sr_{0.3}MnO_3$ onto the Nb:$SrTiO_3$ substrate, a single unit cell of $SrMnO_3$ was deposited to change the termination layer at the interface, creating extra interface dipoles that increase the BC Schottky barrier height[20]. These interface dipoles arise to screen the polar discontinuity at the interface, switching sign for the two different atomic terminations of the Nb:$SrTiO_3$. This suppressed the leakage current by more than four orders of magnitude (Fig. 1c), far below the injection current at the BE junction. For our purposes, $SrMnO_3$ was preferable to SrO insertion, both due to the higher reliability of controlling the interface termination, as well as preserving the height of the BE junction to maximize current transfer (SrO would expose the $La_{0.7}Sr_{0.3}O$ surface at the BE interface). Combining these interface-engineered junctions allows for successful transistor operation at 300 K (Figs. 2 and 3), the first demonstration of a manganite metal-base transistor.

Figure 2a shows a device operating as a hot-electron transistor[10] (HET) in the common-base configuration, where electrons injected from the BE junction pass across the base and above the BC Schottky barrier (Fig. 2e). $I_C$ is measured as a function of the collector voltage ($V_{CB}$) at different fixed values of $I_E$. $\alpha$ is small ($\sim 1.2 \times 10^{-4}$) as shown in Fig. 2b, indicating that while clear transconductance is observed, the current gain is highly attenuated by the short hot-electron mean-free-path, consistent with the low mobility characteristic of manganites. Fig. 2c shows the same device in the common-emitter geometry, where $I_C$ is measured as a function of the collector-emitter voltage ($V_{CE}$) at different fixed values of $I_B$. The deduced common-emitter current gain $\beta$ (~ 1.3 × $10^{-4}$, Fig. 2d), is consistent with the relation $\beta = \alpha / (1 - \alpha)$, confirming HET operation.

Another characteristic feature of HETs is complete electrostatic screening by the base. Because the emitter and collector are separated by the base metal, $V_{CB}$ is fully screened and has no feedback on $V_{EB}$ in the common-base output characteristics. As shown in Fig. 2a, this was indeed observed in the voltage feedback curve. However, the majority of the 53 devices we studied showed varying degrees of voltage feedback. As a representative example, the common-base output characteristics and voltage feedback for a transistor in this regime are shown in Fig. 3a. $\alpha$ significantly depends on $V_{CB}$, ranging from $\alpha = 0.11$ at $V_{CB} = -0.4$ V, to $\alpha = 0.53$ at $V_{CB} = +0.8$ V. These features indicate finite coupling of $V_{EB}$ to $V_{CB}$, which arises despite the same in-plane transport and magnetic properties of the manganite films used as the base layer. Precipitates formed during manganite film growth could be ruled out as the origin of this coupling, since even for films with a high density of precipitates induced by detuning the plume stoichiometry[21], subsequent transistors did not exhibit any statistical increase in voltage feedback. Rather, dilute pinhole defects are the likely origin of this coupling. This is further supported by our electrical measurements which show a connection between emitter and collector, not base/emitter or base/collector.

To elucidate the operating mode of this transistor, temperature dependent measurements were taken between 20 K and 300 K (Fig. 3b). Here $I_C$ is plotted as a function of $V_{EB}$ at $V_{CB}$ = 0 V, which gives the transfer characteristics. At small negative voltage, a linear relationship was observed between log $I_C$ and $V_{EB}$, with increasing slope for decreasing temperature. This thermally-activated process indicates emitter-to-collector current dominated by activation over a barrier, similar to thermionic emission in a Schottky junction[22]. This picture is quantitatively supported by an ideality factor below 2 for all temperatures[18].

The effective emitter-collector barrier can be visualised as the saddle point in the potential contour of the microscopic current path (Fig. 3e), which is characteristic of permeable-base transistors (PBT)[11]. Current transfer in a PBT is determined by a current path controlled by the potential profile in the base. The barrier was quantified by measuring the common-base transfer curves at 10 K for a given $V_{CB}$ varied across ± 0.6 V (Fig. 3c). The effective barrier height ($|V_{EB}|$ at the onset of $I_C$) decreased linearly by applying a positive $V_{CB}$. This variability is a typical feature of PBTs, also causing partial screening in the base (Fig. 3a). The PBT shown in Fig. 3 has significantly higher current gain than the HET in Fig. 2, but still less than unity. By going further into the permeable-base regime, the gain is further increased. Figure 4 shows the case for a PBT with $\alpha$ very close to 1, for which the common-emitter current gain $\beta$ is measured to be ~ 250.

The output characteristics in Fig. 3a can be quantitatively described in a simple model. We define $\Phi(V_{EB}, V_{CB})$ as the effective barrier height with respect to the base (determining emitter-to-collector current transfer), and $\Phi_0 = \Phi(0,0)$ for the unbiased equilibrium state. The linear modulation of $\Phi(V_{EB}, V_{CB})$ by the terminal voltages (Fig. 3c), parameterised by the coupling coefficient $b$, gives

$$\Phi(V_{EB}, V_{CB}) = \Phi_0 - b(V_{EB} + V_{CB}). \quad (1)$$

Since the barrier current and hence $I_C$ is determined by the difference in $\Phi(V_{EB}, V_{CB})$ and $V_{EB}$, $I_C$ can be generalised as

$$I_C = f[\Phi(V_{EB}, V_{CB}) + V_{EB}] \quad (2)$$

by using a suitable function $f[\ ]$, specified below. Combining Eqs. 1 and 2, $I_C = f[\Phi_0 - V_{mix}]$, where $V_{mix} = bV_{CB} - (1-b)V_{EB}$. By optimizing the scaling parameter $b = 0.25$, $I_C$ in the range of $0 \text{ V} < V_{CB} < 0.5 \text{ V}$ can be collapsed onto a single curve as a function of $V_{mix}$ as shown in Fig. 3d. We further note that at high voltages, $I_C \propto V_{mix}^2$, indicating space charge limited current (SCLC) through the current path[23].

Now we can write the functional form for $f[\ ]$ as

$$f[\Phi_0 - V_{mix}] = \begin{cases} I_0 \exp[-q(\Phi_0 - V_{mix})/kT] & (V_{mix} < \Phi_0) \quad (3) \\ A(V_{mix} - \Phi_0)^2 & (\Phi_0 < V_{mix}) \quad (4) \end{cases}$$

where $I_0$ is the prefactor of the exponential behaviour shown in Fig. 3b, $k$ is the Boltzmann constant, and $A$ is the linear coefficient of the SCLC. $\Phi_0$ = 0.65 V for this particular transistor, determined by the intercept in Fig. 3d. Thus this model based on a PBT captures the measured common-base output characteristics of the transistor with partial screening, as parameterised by $b$, $\Phi_0$, and $A$.

Application of the full analysis discussed above to all 53 transistors studied here showed universal scaling as given in Fig. 3d. The resultant parameters $b$ and $\Phi_0$ are plotted in Fig. 5a. When $b \approx 0$, namely $I_C$ is determined by $V_{EB}$ and unaffected by the collector, $\Phi_0$ ~ 0.9 V, the Schottky barrier height of the SrO-terminated $La_{0.7}Sr_{0.3}MnO_3$/Nb:$SrTiO_3$ interface[9]. As $b$ increases and reaches 0.5, $I_C$ is determined purely by $V_{CE}$, and $\Phi_0$ is reduced to a small value. These variations of $b$ and $\Phi_0$ can be seen as the independent consequences of the formation and expansion of the emitter-to-collector current path. When the current path expands, base screening is diminished, resulting in larger $b$ and reduced $\Phi_0$. The two red circles in Fig. 5a correspond to the two representative transistors shown in Figs. 2 and 3. Thus the correlation between $b$ and $\Phi_0$ in Fig. 5a indicates that the dispersion in transistor characteristics measured in all devices can be well described as the evolution from a HET to a PBT.

To corroborate this picture we analyse the dispersion of $\alpha$, which was found to be proportional to $A$ in Eq. 4 (Fig. 5b). In the simple SCLC model, $I_C$ is expressed as $I_C = A(V_{\mathrm{mix}} - \Phi_0)^2 = \frac{9S\varepsilon\mu}{8d^3}(V_{\mathrm{mix}} - \Phi_0)^2$ where $S$ is the cross-sectional area of the current path, $\varepsilon$ is the permittivity, $\mu$ is the carrier mobility, and $d$ is the length of the current path[23]. Assuming $\varepsilon$, $\mu$, and $d$ to be constants, the observed dispersion in $\alpha$ can be attributed to the variation in $S$. The statistical distribution of Fig. 5 is consistent with a very low density of pinhole defects with respect to the device area. Using the simulation results of PBTs from Ref. 11, the maximal pinhole diameter when all transconductance is lost corresponds to ~ 100 nm, consistent with the depletion width in the collector. This indicates that further downscaling of these relatively large structures should shift device yield to the hot-electron regime. Recently developed manganite nanolithography techniques[24] could then be used to controllably tune the base permeability.

In summary, the present work demonstrates a new three-terminal device platform for perovskite oxide heterostructures, which should provide useful for hot-electron spectroscopy of heterostructures incorporating strong electron interactions and quantum wells[25], as well as magnetically active junctions[26]. In the hot-electron regime, the low current gains are far from commercial relevance as basic transistors, and they are comparable to those of metal-base spin-valve transistors[27]. With further improvements, the epitaxial and thermodynamic compatibility of metallic, semiconducting, and other multifunctional states in perovskites may provide an avenue to overcome scattering and defects arising at conventional metal/semiconductor interfaces.

**Methods**

The transistor structure was based on (001)-oriented $SrTiO_3/La_{0.7}Sr_{0.3}MnO_3$/Nb:$SrTiO_3$ trilayers which were grown by pulsed laser deposition[28]. On $TiO_2$-terminated[29] Nb:$SrTiO_3$ (001) substrates with a dopant concentration of 0.01 wt. %, a 20 nm thick $La_{0.7}Sr_{0.3}MnO_3$ base and an 80 nm thick $SrTiO_3$ emitter were consecutively grown at an oxygen partial pressure of $1\times10^{-3}$ Torr. The substrate temperature and the laser fluence were 850 °C and 0.4 J/cm$^2$ for $La_{0.7}Sr_{0.3}MnO_3$ (and the inserted $SrMnO_3$ layer) and 700 °C and 0.6 J/cm$^2$ for $SrTiO_3$. The $SrTiO_3$ layer was deposited through a rectangular template mask. Grown in this manner on $SrTiO_3$ substrates, $SrTiO_3$ films are completely insulating (> 10 GΩ-cm by 4 probe measurement at room temperature). Al/$SrTiO_3$/Nb: $SrTiO_3$ test structures confirmed an Ohmic contact with a contact resistance of ~100 Ω for the dimensions used here. X-ray diffraction studies confirmed high quality epitaxial single crystal thin films which were fully strained to the substrate. Magnetisation measurements gave a Curie temperature of 350 K for the $La_{0.7}Sr_{0.3}MnO_3$ film, similar to that of the bulk[28]. Atomic force microscopy exhibited surfaces with a unit cell step and terrace structure both for $La_{0.7}Sr_{0.3}MnO_3$ and $SrTiO_3$ films. The areas of the BE and BC junctions were 0.1 mm$^2$ and 0.3 mm$^2$. Aluminium and gold electrodes were deposited through shadow masks on the emitter and the base respectively, and indium was contacted by ultrasonic soldering to the collector (substrate). These provide Ohmic contacts with resistances far below the junction impedances in all measurement conditions.

**References:**


1. *The International Technology Roadmap for Semiconductors*: http://www.itrs.net.
2. Takagi, H. & Hwang, H. Y. An emergent change of phase for electronics. *Science* **327**, 1601-1602 (2010).
3. Kahng, D. & Atalla, M. M. in *IEEE-AIEE Solid-State Device Res. Conf.* (Carnegie

Inst. of Tech., Pittsburgh, 1960).

4. Mannhart, J., Schlom, D. G., Bednorz, J. G. & Muller, K. A. Influence of electric fields on pinning in $YBa_2Cu_3O_{7-\delta}$ films. *Phys*. *Rev*. *Lett*. **67**, 2099-2101 (1991).
5. Takahashi, K. S. *et al*. Local switching of two-dimensional superconductivity using the ferroelectric field effect. *Nature* **441**, 195-198 (2006).
6. Ueno, K. *et al*. Electric-field-induced superconductivity in an insulator. *Nat*. *Mater*. **7**, 855-858 (2008).
7. Schockley, W., Sparks, M. & Teal, G. K. *p-n* junction transistors. *Phys*. *Rev*. **83**, 151-162 (1951).
8. Mead, C. A. Operation of tunnel-emission devices. *J*. *Appl*. *Phys*. **32**, 646-652 (1961).
9. Hikita, Y., Nishikawa, M., Yajima, T. & Hwang, H. Y. Termination control of the interface dipole in $La_{0.7}Sr_{0.3}MnO_3$/Nb:$SrTiO_3$ (001) Schottky junctions. *Phys. Rev. B* **79**, 073101 (2009).
10. Sze, S. M., Crowell, C. R., Carey, G. P. & LaBate, E. E. Hot electron transport in semiconductor-metal-semiconductor structures. *J*. *Appl*. *Phys*. **37**, 2690-2695 (1966).
11. Bozler, C. O. & Alley, G. D. Fabrication and numerical simulation of the permeable

base transistor. *IEEE Trans. Electron Devices* ED-**27**, 1128-1141 (1980).

12. Ohtomo, A., Muller, D. A., Grazul, J. L. & Hwang, H. Y. Artificial charge-modulation in atomic-scale perovskite titanate superlattices. *Nature* **419**, 378-380 (2002).

13. Ohtomo, A. & Hwang, H. Y. A high-mobility electron gas at the $LaAlO_3/SrTiO_3$ heterointerface. *Nature* **427**, 423-426 (2004).

14. Smadici, S. *et al*. Electronic reconstruction at $SrMnO_3$-$LaMnO_3$ superlattice interfaces. *Phys*. *Rev*. *Lett*. **99**, 196404 (2007).

15. Gozar, A. *et al*. High-temperature interface superconductivity between metallic and insulating copper oxides. *Nature* **455**, 782-785 (2008).

16. Ahn, C. H., Triscone, J.-M. & Mannhart, J. Electric field effect in correlated oxide systems. *Nature* **424**, 1015-1018 (2003).

17. Bardeen, J. & Brattain, W. H. The transistor, a semi-conductor triode. *Phys*. *Rev*. **74**, 230-231 (1948).

18. Sze, S. M. & Ng, K. K. *Physics of semiconductor devices*, 3rd edn (John Wiley & Sons, Hoboken, 2007).

19. Monsma, D. J., Lodder, J. C., Popma, T. J. A. & Dieny, B. Perpendicular hot electron spin-valve effect in a new magnetic field sensor: the spin-valve transistor.

*Phys*. *Rev*. *Lett*. **74**, 5260-5263 (1995).

20. Capasso, F., Cho, A. Y., Mohammed, K. & Foy, P. W. Doping interface dipoles: Tunable heterojunction barrier heights and band-edge discontinuities by molecular beam epitaxy. *Appl*. *Phys*. *Lett*. **46**, 664-666 (1985).

21. Higuchi, T. *et al*. $Mn_3O_4$ precipitates in laser-ablated manganite films. *Appl*. *Phys*. *Lett*. **95**, 043112 (2009).

22. Crowell, C. R. & Sze, S. M. Current transport in metal-semiconductor barriers. *Solid-Stat. Electron*. **9**, 1035-1048 (1966).

23. Shockley, W. & Prim, R. C. Space-charge limited emission in semiconductors. *Phys*. *Rev*. **90**, 753-758 (1953).

24. Li, R.-W. *et al*. Atomic force microscope lithography in perovskite manganite $La_{0.8}Ba_{0.2}MnO_3$ films. *J*. *Appl*. *Phys*. **95**, 7091-7093 (2004).

25. Hotta, Y. *et al*. Electronic structure of the Mott insulator $LaVO_3$ in a quantum-well geometry. *Appl*. *Phys*. *Lett*. **89**, 251916 (2006).

26. Nakagawa, N. *et al*. Magnetocapacitance and exponential magnetoresistance in manganite-titanate heterojunctions. *Appl*. *Phys*. *Lett*. **86**, 082504 (2005).

27. Jansen, R. *et al*. Thermal spin-wave scattering in hot-electron magnetotransport across a spin valve. *Phys*. *Rev*. *Lett*. **85**, 3277-3280 (2000).

28. Song, J. H., Susaki, T. & Hwang, H. Y. Enhanced thermodynamic stability of epitaxial oxide thin films. *Adv. Mater.* **20**, 2528-2532 (2008).

29. Kawasaki, M. *et al.* Atomic Control of the $SrTiO_3$ crystal surface. *Science* **266**, 1540-1542 (1994).

**Acknowledgements** We thank J. H. Song and C. Bell for discussions. We acknowledge support from the TEPCO Research Foundation, and from the Department of Energy, Office of Basic Energy Sciences, Division of Materials Sciences and Engineering, under contract DE‐AC02‐76SF00515 (H.Y.H.).

**Author Contributions** T.Y. performed device fabrication, measurements, and data analysis. Y.H. and H.Y.H. assisted with the planning, measurements, and analysis of the study.

**Competing interests statement** The authors declare that they have no competing financial interests.

**Correspondence** and requests for materials should be addressed to H.Y.H.

(hyhwang@stanford.edu).

**Figure Captions:**

**Figure 1 | Device fabrication and interface engineering. a**, A schematic illustration of the metal-base transistor with the structure of (001)-oriented $SrTiO_3$(STO)/ $La_{0.7}Sr_{0.3}MnO_3$(LSMO)/Nb:STO. **b**, **c**, Current-voltage characteristics of the base-collector (BC) and the base-emitter (BE) junctions shown for devices without (**b**) and with (**c**) the insertion of a single unit cell of $SrMnO_3$ at the BC interface. Insets show the measurement configuration, and the arrows and triangles indicate typical voltages applied to the junctions during transistor operation.

**Figure 2 | Hot-electron transistor (HET) characteristics at 300 K. a**, Common-base output characteristics and voltage feedback, as $I_E$ is varied from 0 to 1 μA in 0.2 μA steps. **b**, Common-base transfer characteristics for $V_{CB}$ = 0 V. **c**, Common-emitter output characteristics, as $I_B$ is varied from 0 to 1 μA in 0.2 μA steps. **d**, Common-emitter transfer characteristics for $V_{CE}$ = 1.4 V. The common-base current gain $\alpha$ and the common-emitter current gain $\beta$ are calculated from the slopes of the plots in **b** and **d**. **e**, Schematic illustration of the HET.

**Figure 3 | Permeable base transistor (PBT) characteristics. a**, Common-base output characteristics and voltage feedback at 300 K, as $I_E$ is varied from 0 to 1 μA in 0.2 μA steps. **b**, **c**, Temperature dependence (**b**, 20 K intervals, $V_{CB}$ = 0 V) and $V_{CB}$ dependence (**c**, 0.2 V intervals, 10 K) of the common-base transfer characteristics. **d**, Scaling plot of the square root of the collector current ($I_C$) as a function of $V_{mix}$, for the optimum scaling parameter $b$ = 0.25. The intercept gives the unbiased effective barrier height, $\Phi_0$ = 0.65 V. **e**, Schematic illustration of the PBT.

**Figure 4 | Permeable base transistor (PBT) in the high gain regime ($\alpha$ ~ 1). a**, Common-base output characteristics and voltage feedback at 300 K, as $I_E$ is varied from 0 to 1 μA in 0.2 μA steps. **b**, Common-emitter current transfer characteristics $I_C$ versus $I_B$ (at $V_{CE}$ = 1.4 V), for which $\beta$ ~ 250 for $I_C$ ~ 0.

**Figure 5 | Evolution of transistor operation. a**, Correlation between the unbiased effective barrier height ($\Phi_0$) and the voltage transfer between the emitter and the collector ($b$). **b**, Correlation between the linear coefficient in SCLC ($A$) and the current gain ($\alpha$). In **a** and **b**, the distribution of transistor characteristics at 300 K for all 53 measured transistors are given. The dashed curves and line are guides to the eye. **c**, **d**, Schematic illustrations of the current transfer for the HET and the PBT.

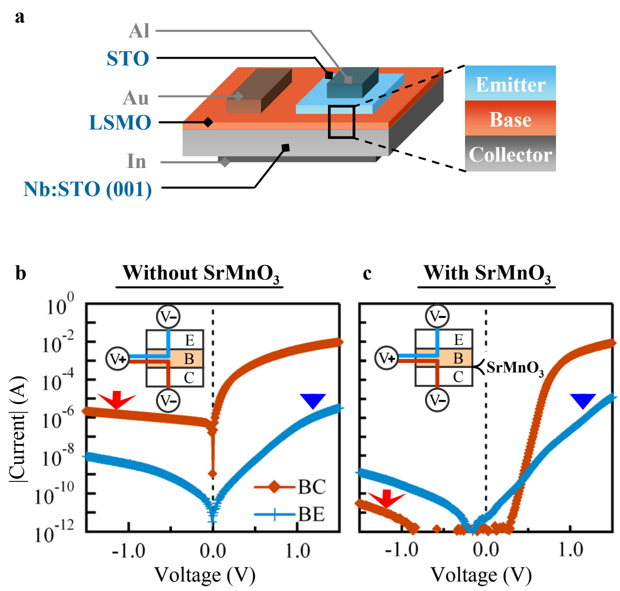


**Figure 1 T. Yajima *et al.***

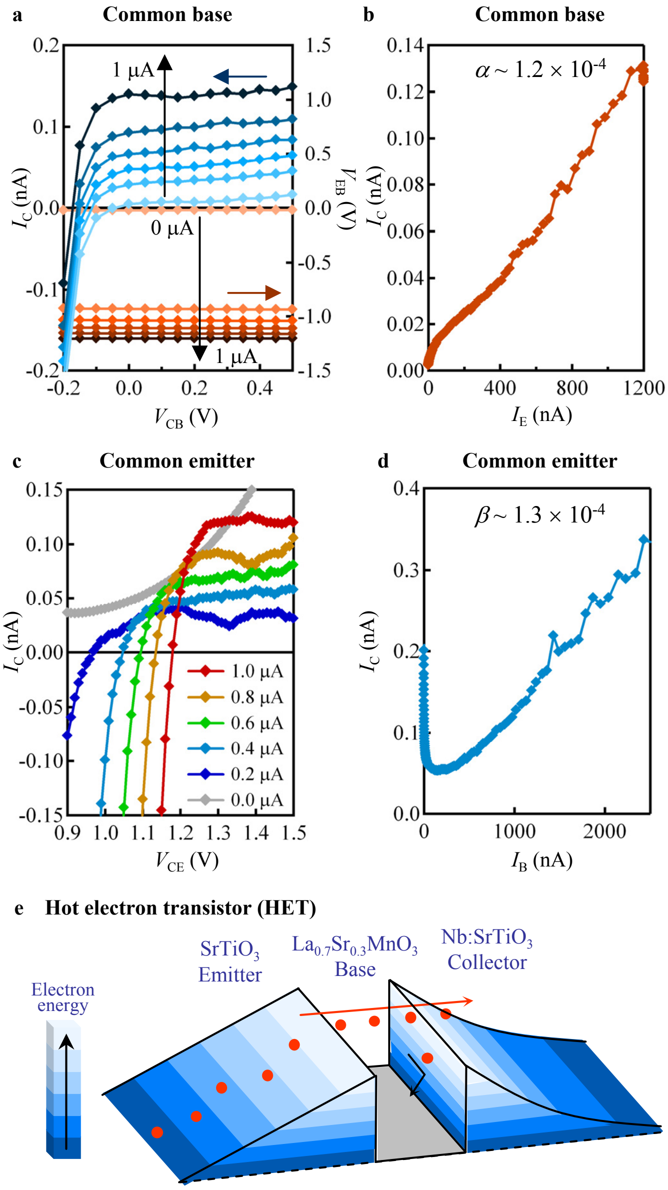


**Figure 2 T. Yajima *et al.***

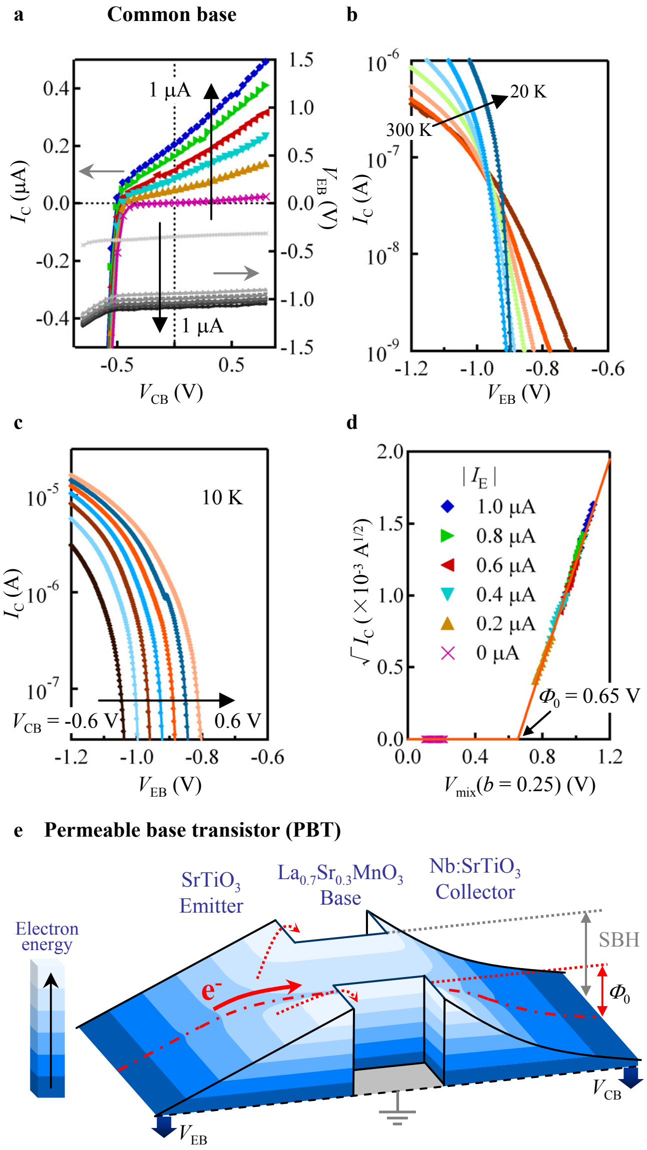


**Figure 3 T. Yajima *et al.***

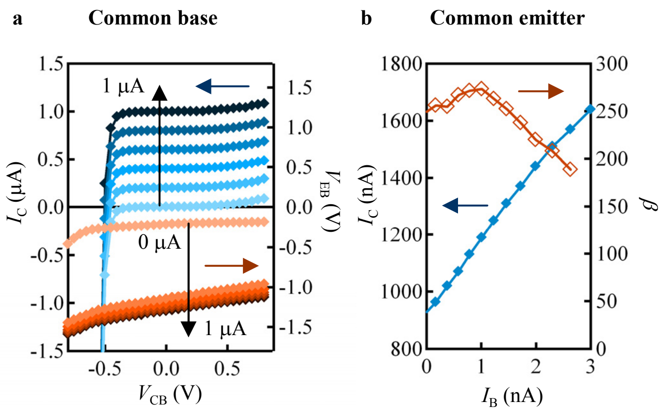


**Figure 4 T. Yajima *et al.***

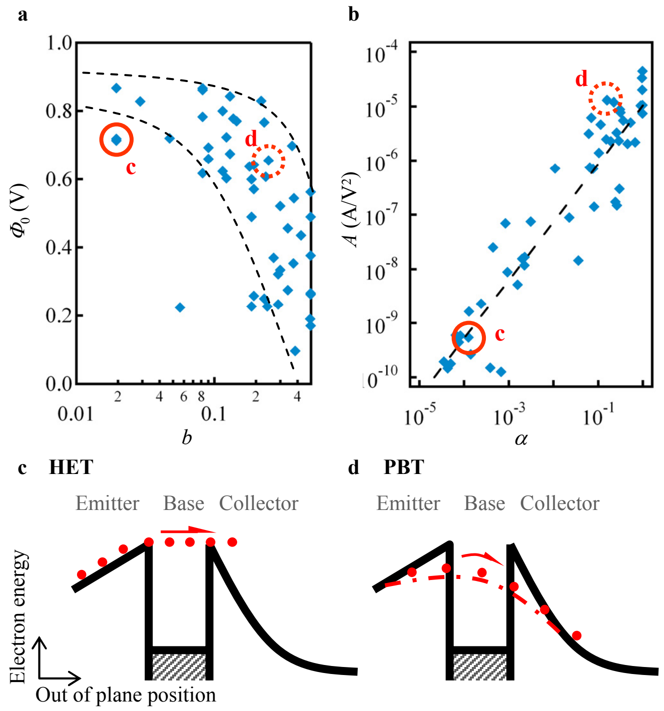


**Figure 5 T. Yajima *et al.***